Low-Complexity Sub-band Divided Ray Tracing for UWB Indoor Channels

Mingming Gan[1], Paul Meissner[2], Francesco Mani[3], Erik Leitinger[2],
Markus Fröhle[4], Claude Oestges[5], Klaus Witrisal[2], Thomas Zemen[1]
[1]FTW Forschungszentrum Telekommunikation Wien, Austria; [2] Graz University of Technology, Austria;
[3] COMELEC Department, Telecom ParisTech, France; [4] Chalmers University of Technology, Sweden;
[5] ICTEAM, Université catholique de Louvain, Belgium

***Abstract*—Ray tracing has been extensively used to simulate indoor channel characteristics. For an ultra-wideband system, the channel characteristics vary significantly over the entire bandwidth. To cope with this, sub-band divided RT has been proposed by dividing the frequency of interest into multiple subbands and superposing the RT results at the individual center frequency of each subband. Thus, the computational complexity is directly proportional to the number of subbands. In this paper, we propose a mathematical method to significantly reduce the computational complexity of the sub-band divided RT, making it almost independent of the number of subbands. It is important to note that, based on our approach, not only the determination of the rays reaching a give location is made only once, but also the electromagnetic calculation of the received signal is not needed to perform repeatedly. The accuracy of low-complexity sub-band divided RT algorithm is verified through a measurement campaign.**

***Keywords*—ray tracing, ultra-wideband, channel modeling, indoor, low-complexity.**

I. Introduction

UWB technology has attracted a lot of interest in recent years as an ideal candidate for short-range and broadband indoor wireless communication systems. It offers major enhancements in multiple wireless application areas. One important area refers to the localization in indoor environments by UWB systems enabling a fine delay resolution of the multipath components of the received signal [1], [2]. The achieved accuracy of localization methods based on the radio signal is strongly affected by the propagation channel. Therefore, it is crucial to understand the UWB channel properties. Two main categories of channel modeling techniques for UWB channels exist [3]: one is the statistical modeling based on frequency or time domain measurements, the other is deterministic modeling based on a scenario map. So far, sub-band divided RT has been frequently employed as the typical deterministic channel modeling tool for UWB indoor channels by the superposition of RT results implemented at the individual center frequency of each subband [4], [5].

It is evident that the computational complexity of RT depends on the number of propagation paths considered. Moreover, it has been experimentally shown that diffuse scattering components are an important factor in determining time and angle dispersion of radio signals in indoor environments [6]. The inclusion of the diffuse scattering mechanism in RT introduces a large number of propagation paths in an indoor environment, which makes the calculation of the electromagnetic characteristics extremely time-consuming.

Conventional sub-band divided RT simulation obviously makes the computation procedure more complicated and leads to the computation time being directly proportional to the number of frequency points. Although some simplifications have been made for sub-band divided RT by determining the relevant propagation paths once at the beginning of the procedure, the electromagnetic calculation of the received signal still needs to be performed repeatedly at different individual frequency points [7]. Furthermore, extracting the statistics of the channel requires that sub-band divided RT simulations must be performed for a large number of positions, which would result in unacceptable long simulation time.

In order to significantly improve the computational efficiency of sub-band divided RT for UWB indoor systems, we make the following contributions in this paper:

- Based on the electromagnetic propagation mechanisms, a low-complexity sub-band divided RT algorithm is derived. As a major enhancement, not only the geometric calculation, but also the electromagnetic calculation only needs to be performed once for all subbands.
- For the diffuse scattering case, we show numerical simulation results to verify that the subdivision of rough surfaces at the center frequency of the entire bandwidth is valid for all subbands.
- The accuracy of the proposed low-complexity algorithm is justified by comparing with the conventional sub-band divided RT. Moreover, increasing the number of subbands can obtain a slightly higher correlation with the measurement but without increasing much simulation time.

The author would like to thank Miss Xuhong Li for assistance with speeding up the ray tracing simulation. The work of M. Gan and T. Zemen is supported by the Austrian Science Fund (FWF) through grant NFN SISE (S10607) and by the Austrian Competence Center FTW Forschungszentrum Telekommunikation Wien GmbH within project I0. FTW is funded within the program COMET - Competence Centers for Excellent Technologies by BMVIT, BMWFJ, and the City of Vienna. The COMET program is managed by the FFG. The work of P. Meissner, E. Leitinger and K. Witrisal was partly supported by the Austrian Science Fund (FWF) within the National Research Network SISE (S10610), and by the Austria Research Promotion Agency (FFG) within KIRAS PL3, grant nb. 832335 "LOBSTER". This collaboration was also part of the COST action IC1004 entitled "Cooperative Radio Communications for Green Smart Environments".

The paper is organized as follows: Section II describes the RT channel model based on the electromagnetic illumination and the low-complexity algorithm, which significantly reduces the simulation time. Section III presents the measurement campaign and RT setup. Simulation results of the proposed algorithm are given in Section IV. Finally, we conclude in Section V.

II. RT Channel Model

The RT tool employed in the present work is for three-dimensional (3D) environment and three major wave propagation mechanisms are taken into account: (i) line of sight (LOS), (ii) specular components as well as (iii) diffuse scattering [8]. The specular components contain reflection, penetration and diffraction contributions. A thorough geometrical and electromagnetic description of the indoor environment, as well as the radiation properties of the antennas are required for calculating the propagation paths connecting the transmitter (Tx) and the receiver (Rx) locations. RT enables the calculation of the electric field parameters in amplitude, phase and polarization at the mobile terminal position relying upon the relevant propagation mechanisms [9].

A. Sub-band Divided RT

The sub-band divided RT algorithm applied to UWB radio channels has been introduced in [4], [5]. The basic steps of the method can be summarized as follow:

- The entire UWB bandwidth B is divided into multiple subbands B_i, where i is the index of the subband with $i \in \{1, \cdots, I\}$ and I is the total number of the subands.
- Conventional RT is implemented to obtain the corresponding channel impulse response (CIR) $h_i(\tau)$ at the center frequency $f_{\mathrm{c},i}$ of each subband i, where τ is the propagation path delay.
- The channel transfer function (CTF) at each subband i is obtained by Fourier transform. Then CTFs of all subbands are combined together for the entire bandwidth.
- An inverse Fourier transform yields the overall CIR $h(\tau)$ for the entire bandwidth.

B. Low-Complexity Sub-band Divided RT

The CIR at each subband i is directly determined by the propagation mechanisms. The LOS components is only affected by the free-space loss, while the specular components are calculated in a similar way referring to the relevant complex dyadic coefficients and the total length of the path. The reflection and penetration coefficients are calculated by the Fresnel formulas [10], whereas the diffraction coefficient is obtained using the uniform theory of diffraction [11]. It is assumed that the path direction is not modified by the penetration mechanism in our RT tool [12]. Moreover, it is known that a flat wave is scattered into multiple random directions when it is interacting with a rough surface. A directive scattering pattern model is used in our RT tool to evaluate the amplitude of each diffuse scattering path, which assumes the scattering lobe is steered towards the direction of the specular reflection [6], [12]. The detailed formulas of the propagation mechanisms are introduced in Appendix, from which it is apparent to see which parameters are varying with the frequency. Therefore, the electromagnetic calculations $E_{\{\cdot\}}(f_{\mathrm{c},i'})$ at other sub-bands $f_{\mathrm{c},i'}$, where $i' \in \{1, \cdots, I\}$, for one Rx position can be derived from the electromagnetic results $E_{\{\cdot\}}(f_{\mathrm{c},i})$ of one sub-band $f_{\mathrm{c},i}$.

- For the LOS component, the electric field at a different sub-band i' can be obtained directly

$$E_{\mathrm{LOS}}(f_{\mathrm{c},i'}) = E_{\mathrm{LOS}}(f_{\mathrm{c},i}) \cdot \left[\frac{\bar{g}^{\mathrm{R}}_{\mathrm{LOS}}(f_{\mathrm{c},i'})}{\bar{g}^{\mathrm{R}}_{\mathrm{LOS}}(f_{\mathrm{c},i})}\right]^* \cdot \frac{f_{\mathrm{c},i}}{f_{\mathrm{c},i'}} \cdot \left[\frac{\bar{g}^{\mathrm{E}}_{\mathrm{LOS}}(f_{\mathrm{c},i'})}{\bar{g}^{\mathrm{E}}_{\mathrm{LOS}}(f_{\mathrm{c},i})}\right] e^{\frac{-j2\pi(f_{\mathrm{c},i'} - f_{\mathrm{c},i})s_{\mathrm{LOS}}}{c}}, \tag{1}$$

  where c is the speed of light, s_{LOS} is the distance between the Tx and Rx, $\bar{g}^{\mathrm{E}}_{\{\cdot\}}(f_{\mathrm{c},\{\cdot\}}) = \bar{g}^{\mathrm{E}}_{\{\cdot\}}(f_{\mathrm{c},\{\cdot\}}, \theta_{\mathrm{E}}, \phi_{\mathrm{E}})$ and $\bar{g}^{\mathrm{R}}_{\{\cdot\}}(f_{\mathrm{c},\{\cdot\}}) = \bar{g}^{\mathrm{R}}_{\{\cdot\}}(f_{\mathrm{c},\{\cdot\}}, \theta_{\mathrm{R}}, \phi_{\mathrm{R}})$ are the complex vectors accounting for the Tx/Rx antenna polarization and amplitude gains within one subband in the direction of the propagation wave, $\theta_{\{\cdot\}}$ and $\phi_{\{\cdot\}}$ indicate the azimuth and elevation directions of the transmitted/received wave, and $\{\cdot\}^*$ designates the complex conjugate. It is worth mentioning that the geometrical calculation of each propagation ray is identical at different subbands, so that the corresponding $\theta_{\{\cdot\}}$ and $\phi_{\{\cdot\}}$ of the wave is constant for all subbands. In order to simplify the expressions, we omit the arguments $\theta_{\{\cdot\}}$ and $\phi_{\{\cdot\}}$ in the related formulas.
- In [7], [13], it is assumed that the dielectric permittivity ε_r and conductivity σ for one material are independent of the frequencies within the entire bandwidth of interest, because it is difficult to estimate how these values vary with the frequency. However, the effective permittivity of the material

$$\varepsilon_{r,\mathrm{eff}}(f_{\mathrm{c},i}) = \varepsilon_r - j\sigma/(2\pi f_{\mathrm{c},i}\varepsilon_0) \tag{2}$$

  where ε_0 is the permittivity of vacuum, is still varying with the frequencies in these literatures. Here we fix the effective permittivity $\varepsilon_{r,\mathrm{eff}}$ for the entire UWB bandwidth. Therefore, the Fresnel reflection/penetration coefficients are independent of frequency, which is justified in the numerical results. As a consequence, the electric field of the reflection/penetration contribution at a different subband i' can be computed as

$$E_{\mathrm{r/p}}(f_{\mathrm{c},i'}) = E_{\mathrm{r/p}}(f_{\mathrm{c},i}) \cdot \left[\frac{\bar{g}^{\mathrm{R}}_{\mathrm{r/p}}(f_{\mathrm{c},i'})}{\bar{g}^{\mathrm{R}}_{\mathrm{r/p}}(f_{\mathrm{c},i})}\right]^* \cdot \frac{f_{\mathrm{c},i}}{f_{\mathrm{c},i'}} \cdot \left[\frac{\bar{g}^{\mathrm{E}}_{\mathrm{r/p}}(f_{\mathrm{c},i'})}{\bar{g}^{\mathrm{E}}_{\mathrm{r/p}}(f_{\mathrm{c},i})}\right] e^{\frac{-j2\pi(f_{\mathrm{c},i'} - f_{\mathrm{c},i})(s_{\mathrm{r/p}} + s'_{\mathrm{r/p}})}{c}}, \tag{3}$$

  where $s_{\mathrm{r/p}}$ is the path length from Tx to the reflection point and $s'_{\mathrm{r/p}}$ is the path length from the reflection point to the Rx.

- For the diffracted contribution, it can be seen in Appendix that the dyadic diffraction coefficients $D_{\parallel}^{\perp}$ are influenced by the frequency. Actually, the dyadic diffraction coefficients can be simplified by ignoring the involved transition functions' effect. The reason is that only one of the arguments in the four transition functions is smaller than 10 for one diffraction point, so that only one of the transition values is different from unity [14]. According to (13) in Appendix, it is acceptable to assume that the value of each transition function referred in D_1, D_2, D_3 or D_4 is the same for one diffraction point at different sub-bands. Therefore, the electric field of the diffraction path at a different sub-band i' can be obtained as

$$E_{\mathrm{d}}(f_{\mathrm{c},i'}) = E_{\mathrm{d}}(f_{\mathrm{c},i}) \cdot \left[\frac{\bar{g}_{\mathrm{d}}^{\mathrm{R}}(f_{\mathrm{c},i'})}{\bar{g}_{\mathrm{d}}^{\mathrm{R}}(f_{\mathrm{c},i})}\right]^{*} \cdot \left(\frac{f_{\mathrm{c},i}}{f_{\mathrm{c},i'}}\right)^{\frac{3}{2}} \cdot \left[\frac{\bar{g}_{\mathrm{d}}^{\mathrm{E}}(f_{\mathrm{c},i'})}{\bar{g}_{\mathrm{d}}^{\mathrm{E}}(f_{\mathrm{c},i})}\right] e^{\frac{-j2\pi(f_{\mathrm{c},i'}-f_{\mathrm{c},i})(s_{\mathrm{d}}+s_{\mathrm{d}}')}{c}}, \tag{4}$$

  where s_{d} is the path length from Tx to the diffraction point and s_{d}' is the path length from the diffraction point to the Rx.
- A surface appears rougher with increasing frequency, which should result in a denser subdivision of the surface for subbands with higher center frequencies. However, this significantly increases the computational effort. In [13], the subdivision of each surface for a specific Rx position at the center frequency of the entire bandwidth is assumed to be valid for all subbands. Here it is shown that this assumption is reasonable according to the comparison given in Fig.2 in Section III. Thus, the electric field for the scattering path at a different subband i' can be calculated as

$$E_{\mathrm{s}}(f_{\mathrm{c},i'}) = E_{\mathrm{s}}(f_{\mathrm{c},i}) \cdot \left[\frac{\bar{g}_{\mathrm{s}}^{\mathrm{R}}(f_{\mathrm{c},i'})}{\bar{g}_{\mathrm{s}}^{\mathrm{R}}(f_{\mathrm{c},i})}\right]^{*} \cdot \frac{f_{\mathrm{c},i}}{f_{\mathrm{c},i'}} \cdot \left[\frac{\bar{g}_{\mathrm{s}}^{\mathrm{E}}(f_{\mathrm{c},i'})}{\bar{g}_{\mathrm{s}}^{\mathrm{E}}(f_{\mathrm{c},i})}\right] e^{-j\theta_{\mathrm{s}}'}, \tag{5}$$

  where θ_{s}' is the random phase with an uniform distribution in $[0, 2\pi]$.

It should be noted that the above formulas can also be extended for the multi-order propagation path case by combing the results of corresponding propagation mechanisms.

III. Measurement Campaign and RT Setup

A. Measurement Campaign

Frequency-domain UWB channel measurements were carried out by the Signal Processing and Speech Communication laboratory at Graz University of Technology [15]. The size of the scenario is about 29m $\times$ 7.1m $\times$ 10.5m. It consists primarily of concrete walls, glass windows and metal pillars. The locations of the Tx antenna was fixed, while the Rx antennas formed a grid with 22×22 points with 5cm spacing resulting in a total area of 1m $\times$ 1m. A Rhode & Schwarz ZVA-24 vector network analyzer (VNA) was used to measure the CTF at 7501 frequency points over the frequency range from 3.1 to 10.6GHz.

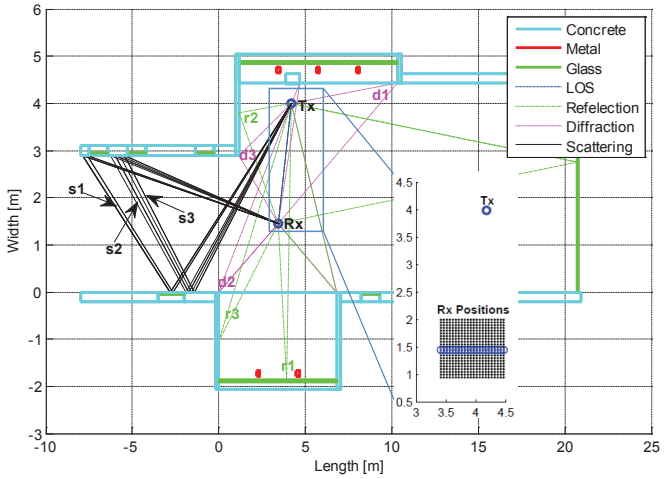

Fig. 1. 2-D top view of measurements environment including a close-up view of the grid Rx's positions together with the positions marked in blue line where RT simulations are implemented.

B. RT Setup

A 2-D top view of the scenario is shown in Fig.1, the different materials are sketched with different colors. The dielectric properties are also included in the input database of RT, where a metallic block is considered as a perfect electric conductor. The values for other materials are: $\varepsilon_r = 6$ and $\sigma = 0.08$ S/m for concrete blocks, and $\varepsilon_r = 5.5$ and $\sigma = 0$ S/m for glass blocks, respectively. The Tx and Rx antennas used for the RT simulation are the dipole antennas corresponding to the antennas used in measurements. RT simulations are implemented at the middle horizontal line of the grid marked in blue in Fig. 1. Moreover, the entire bandwidth B of 7.5GHz is divided into $I = 15$ sub-bands with $B_i = 500$MHz each in our simulation. The involved propagation mechanisms

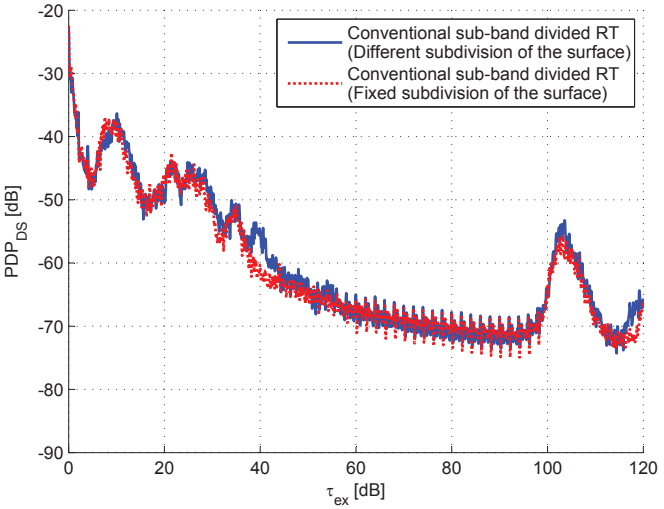

Fig. 2. PDP of the diffuse scattering paths $\mathrm{PDP}_{\mathrm{DS}}$ with different and the subdivisions at different subbands relying on conventional sub-band divided RT.

are LOS, reflection up to the third order, penetration, single diffraction, diffuse scattering, where the penetration contribution has been embedded into all other mechanisms. The diffuse scattering components include single bounce scattering, scattering-reflection and reflection-scattering cases. Some propagation paths are visualized in Fig.1, some of which are indexed by the corresponding number, where **r** indicates the reflection component, **d** means the diffraction component and **s** implies the diffuse scattering component.

Based on our numerical implementation, we compare the power delay profile (PDP) of the diffuse scattering paths $\mathrm{PDP_{DS}}$, with different and fixed subdivision of tile at different subbands relying on the conventional sub-band divided RT. The $\mathrm{PDP_{DS}}$ is obtained by averaging the normalized CIRs at the selected 22 Rx's locations, taking only the diffuse scattering components into account. Note that the $\mathrm{PDP_{DS}}$ is defined over the excess delay τ_{ex}. The result is shown in Fig. 2, from which it can be seen that the $\mathrm{PDP_{DS}}$ based on the fixed subdivision at 6.85GHz over the whole bandwidth is similar to the one where the subdivision is changed according to the center frequency of each subband. Therefore, (5) is a valid approximation for the diffuse scattering case of the low-complexity sub-band divided RT.

IV. Numerical Results

A. Amplitude and Phase Comparison

The comparison of amplitude and phase of propagation paths based on the conventional sub-band divided RT and low-complexity sub-band divided RT is shown in Fig.3, where the corresponding results at the center point of the simulated Rx positions is taken as an example. The selected paths correspond to the indexed paths indicated in Fig.1. It can be seen that the amplitude of each path is decreasing with the increasing subband center frequency $f_{\mathrm{c},i}$. For LOS and specular components, the amplitude and phase of each path based on the conventional sub-band divided RT match well with the results calculated by the low-complexity algorithm. For diffuse scattering components, the amplitude matches well while the phase does not match as a result of the random phases of the rough surfaces.

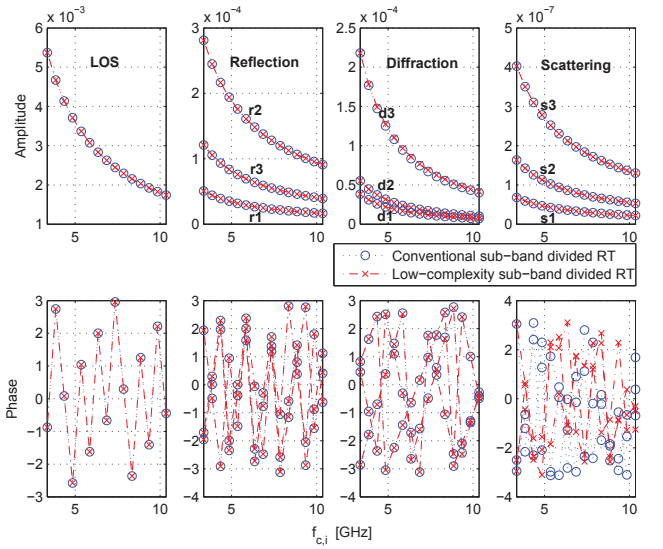

Fig. 3. Amplitude and phase comparison results of propagation paths based on the conventional sub-band divided RT and low-complexity sub-band divided RT. The results shown here correspond to the indexed propagation paths indicated in Fig.1.

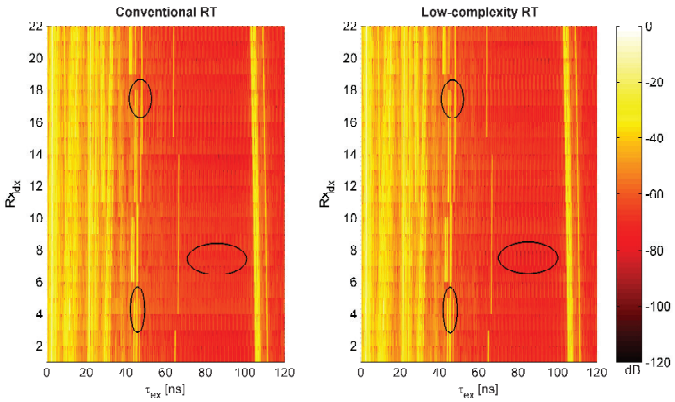

Fig. 4. Comparison of normalized CIRs at the selected 22 Rx's locations based on the conventional sub-band divided RT and low-complexity sub-band divided RT. Some small deviations are highlighted by ellipses.

B. Normalized CIR Comparison

For comparison, the normalized CIRs $h(\tau)$ at the selected 22 Rx's locations, indicated by $\mathrm{Rx_{idx}}$, are shown in Fig. 4 based on the conventional sub-band divided RT and low-complexity sub-band divided RT, respectively. It can be seen that the specular components are mainly located between 0ns and 45ns, and 102ns and 112ns for our scenario. In general, the obtained CIRs based on the conventional sub-band divided RT and low-complexity sub-band divided RT are comparable to each other even though small deviations exist, some of which are highlighted in Fig. 4. The main reason caused the small deviations is evaluated as follow: for the reflection/penertration case, the error is introduced by the assumption that the effective permittivity $\varepsilon_{r,\mathrm{eff}}$ is assumed to be independent of the frequency; for the diffraction case, the reason is the presumable same value of each transition function referred in D_1, D_2, D_3 or D_4 for one diffraction point at different sub-bands. For the scattering case, the error results from by the parameter U in (5), which further shows that the error is also related to the the effective permittivity $\varepsilon_{r,\mathrm{eff}}$. It is worth mentioning that the random phase components are set the same in these two sub-band divided RT simulations for the same Rx position. Therefore, the deviation caused by the random phases has been removed.

C. Simulation Time and PDP Comparison

The simulation time of the low-complexity sub-band divided RT for one Rx's location is about 222s (2.4GHz Intel Core i7 CPU with 8GB RAM), while the conventional sub-band divided RT takes about 3284s, which means that the computa-

tional time can be reduced by a factor of 15. In [16], it is mentioned that the larger the number of the subbands the slightly better is the accuracy of RT for the millimeter wave indoor communication channels, but at the cost of the computational time. In terms of our proposed low-complexity algorithm for the UWB indoor scenario, the effect of computational time can be ignored when choosing the number of subbands. In Fig. 5, the normalized PDPs are compared by averaging the absolute square values of the normalized CIRs over the positions where RT simulations are available. The reason for the gap between the measurements and RT simulations is that (i) priori approximation of the input material parameters got from literature are used, (ii) some small stuffs are not considered in this large dimensions' environment, and (iii) higher-order propagation mechanisms are not considered by the RT algorithm. The correlation coefficients of the different PDPs are also calculated: it is 0.9830 between the low-complexity subband divided RT within 15 subbands and the measurements, while it is 0.9833 between the low-complexity subband divided RT within 50 subbands and the measurements. Therefore, we conclude that the PDPs calculated though the sub-band divided RT and low-complexity sub-band divided RT within 15 subbands are almost the same, while further increasing the number of subbands does not increase the simulation time much.

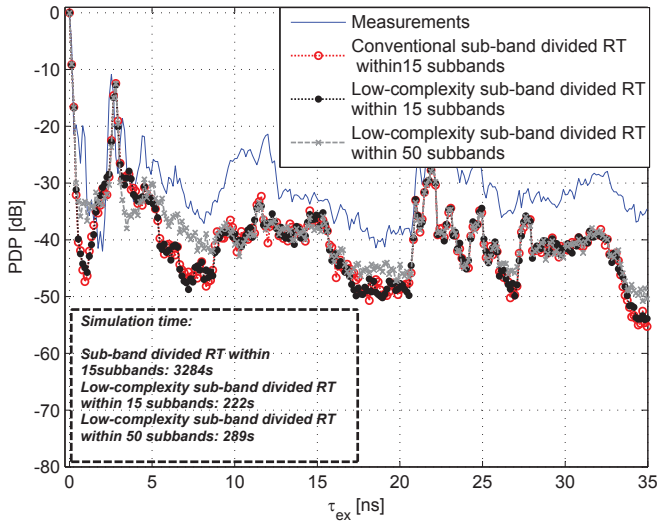

Fig. 5. Normalized PDP comparison based on measurements, conventional sub-band divided RT, low-complexity sub-band divided RT with 15 subbands, low-complexity sub-band divided RT with 50 subbands.

V. Conclusion

In this paper, we presented a low-complexity sub-band divided RT for UWB indoor channels. The algorithm is derived from the electromagnetic illumination of the propagation paths base on two important assumptions: (i) the effective permittivity of each material and (ii) the transfer function referred in the dyadic diffraction coefficient are independent of the frequency for the UWB frequency range. According to our approach, not only the geometrical calculation, but also the electromagnetic calculation of the propagation paths at one specific location needs to be performed only once. Therefore, a reduction of the computational complexity by a factor equal to the number of subbands, can be achieved. Furthermore, the normalized PDPs of the conventional sub-band divided RT and low-complexity sub-band divided RT are comparable to each other. Based on the proposed implementation, we can increase the number of subbands without increasing simulation time. In future work, we will present that this low-complexity algorithm can help to calibrate the RT results by optimizing the material parameters, including the permittivity, conductivity and scattering parameters.

Appendix

The LOS component at one subband i is represented as

$$E_{\mathrm{LOS}}(f_{\mathrm{c},i}) = A(f_{\mathrm{c},i})[\bar{g}^{\mathrm{R}}_{\mathrm{LOS}}(f_{\mathrm{c},i})]^* \cdot [\bar{g}^{\mathrm{E}}_{\mathrm{LOS}}(f_{\mathrm{c},i})] e^{\frac{-j2\pi f_{\mathrm{c},i} s_{\mathrm{LOS}}}{c}} E_0, \tag{6}$$

where $A(f_{\mathrm{c},i}) = c/(4\pi f_{\mathrm{c},i} s)$ is the free space pathloss and s is the total path length between Tx and Rx, where $s = s_{\mathrm{LOS}}$, and E_0 is the emitted field.

For a single reflection/penetration component at one subband i, the electric field can be expressed as

$$\begin{aligned} E_{\mathrm{r/p}}(f_{\mathrm{c},i}) =& A(f_{\mathrm{c},i})[\bar{g}^{\mathrm{R}}_{\mathrm{r/p}}(f_{\mathrm{c},i})]^* \cdot \\ & \overline{\overline{\mathbf{T}}}(f_{\mathrm{c},i}) \cdot [\bar{g}^{\mathrm{E}}_{\mathrm{r/p}}(f_{\mathrm{c},i})] e^{\frac{-j2\pi f_{\mathrm{c},i}(s\mathrm{r/p}+s'\mathrm{r/p})}{c}} E_0, \end{aligned} \tag{7}$$

where $s = s_{\mathrm{r/p}} + s'_{\mathrm{r/p}}$ and $\overline{\overline{\mathbf{T}}}$ is the Fresnel reflection/penetration coefficient [9], [12], which is decomposed into perpendicular and parallel polarization coefficients separately

$$R_\perp = \frac{\cos\vartheta_{\mathrm{inc}} - \sqrt{\varepsilon_{r,\mathrm{eff}} - \sin^2\vartheta_{\mathrm{inc}}}}{\cos\vartheta_{\mathrm{inc}} + \sqrt{\varepsilon_{r,\mathrm{eff}} - \sin^2\vartheta_{\mathrm{inc}}}}, \tag{8}$$

$$R_\parallel = \frac{\varepsilon_{r,\mathrm{eff}}\cos\vartheta_{\mathrm{inc}} - \sqrt{\varepsilon_{r,\mathrm{eff}} - \sin^2\vartheta_{\mathrm{inc}}}}{\varepsilon_{r,\mathrm{eff}}\cos\vartheta_{\mathrm{inc}} + \sqrt{\varepsilon_{r,\mathrm{eff}} - \sin^2\vartheta_{\mathrm{inc}}}}, \tag{9}$$

$$P_\perp = \frac{2\cos\vartheta_{\mathrm{inc}}}{\cos\vartheta_{\mathrm{inc}} + \sqrt{\varepsilon_{2r,\mathrm{eff}}/\varepsilon_{1r,\mathrm{eff}} - \sin^2\vartheta_{\mathrm{inc}}}}, \tag{10}$$

$$P_\parallel = \frac{2\sqrt{\varepsilon_{1r,\mathrm{eff}}/\varepsilon_{2r,\mathrm{eff}}}\cos\vartheta_{\mathrm{inc}}}{\cos\vartheta_{\mathrm{inc}} + \sqrt{\varepsilon_{1r,\mathrm{eff}}/\varepsilon_{2r,\mathrm{eff}}(1 - \varepsilon_{1r,\mathrm{eff}}/\varepsilon_{2r,\mathrm{eff}}\sin^2\vartheta_{\mathrm{inc}})}}, \tag{11}$$

where ϑ_{inc} is the incident angle.

For a diffracted component at one subband i, the electric field is calculated as

$$\begin{aligned} E_{\mathrm{d}}(f_{\mathrm{c},i}) =& A(f_{\mathrm{c},i})[\bar{g}^{\mathrm{R}}_{\mathrm{d}}(f_{\mathrm{c},i})]^* \cdot \\ & \overline{\overline{\mathbf{D}}}(f_{\mathrm{c},i}) \cdot [\bar{g}^{\mathrm{E}}_{\mathrm{d}}(f_{\mathrm{c},i})] \sqrt{\frac{s_{\mathrm{d}} + s'_{\mathrm{d}}}{s_{\mathrm{d}} s'_{\mathrm{d}}}} e^{\frac{-j2\pi f_{\mathrm{c},i}(s_{\mathrm{d}}+s'_{\mathrm{d}})}{c}} E_0, \end{aligned} \tag{12}$$

where $s = s_\mathrm{d} + s'_\mathrm{d}$ and $\overline{\overline{\mathbf{D}}}$ is the dyadic diffraction coefficient, which also can be decomposed into perpendicular and parallel polarization coefficients separately

$$D_{\|}^{\perp} = \frac{-e^{-j\pi/4}}{4n\pi\sqrt{f_{\mathrm{c},i}/c}\sin\beta_0}[D_1 + D_2 + R_{0\|}^{\perp}D_3 + R_{n\|}^{\perp}D_4], \tag{13}$$

where $n = 2 - \alpha/\pi$, α is the interior wedge angle, so that $n\pi$ is the exterior angle of the wedge, β_0 is the angle between the incident wave and the edge, $R_{0\|}^{\perp}$ and $R_{n\|}^{\perp}$ are the reflection coefficients for either perpendicular or parallel polarization for the $0-$face and $n-$face, which are labeled two faces of one wedge [11], and

$$D_1 = \cot(\frac{\pi + (\vartheta_{\text{diff}} - \vartheta_{\text{inc}})}{2n}) \cdot F(\frac{2\pi f_{\mathrm{c},i}}{c} La^{+}(\vartheta_{\text{diff}} - \vartheta_{\text{inc}})), \tag{14}$$

$$D_2 = \cot(\frac{\pi - (\vartheta_{\text{diff}} - \vartheta_{\text{inc}})}{2n}) \cdot F(\frac{2\pi f_{\mathrm{c},i}}{c} La^{-}(\vartheta_{\text{diff}} - \vartheta_{\text{inc}})), \tag{15}$$

$$D_3 = \cot(\frac{\pi + (\vartheta_{\text{diff}} + \vartheta_{\text{inc}})}{2n}) \cdot F(\frac{2\pi f_{\mathrm{c},i}}{c} La^{+}(\vartheta_{\text{diff}} + \vartheta_{\text{inc}})), \tag{16}$$

$$D_4 = \cot(\frac{\pi - (\vartheta_{\text{diff}} + \vartheta_{\text{inc}})}{2n}) \cdot F(\frac{2\pi f_{\mathrm{c},i}}{c} La^{-}(\vartheta_{\text{diff}} + \vartheta_{\text{inc}})), \tag{17}$$

where

$$F(x) = 2j\sqrt{x}e^{jx}\int_{\sqrt{x}}^{\infty} e^{-ju^2}du, \tag{18}$$

is the transition function, which involves a Fresnel integral. If the argument of the function exceeds 10, the (18) can be replaced by unity [14], and

$$L = \frac{s_\mathrm{d}s'_\mathrm{d}}{s_\mathrm{d} + s'_\mathrm{d}}\sin^2\beta_0, \tag{19}$$

$$a^{\pm}(\xi) = 2\cos^2(\frac{2n\pi N^{\pm} - \xi}{2}), \tag{20}$$

where $N^{\pm}$ are the integers which most closely satisfy the equation $2n\pi N^{\pm} - \xi = \pm\pi$.

For the diffuse scattering components, the rough surface needs to be divided into multiple tiles firstly, from the center of which the diffuse scattering path is supposed to originate. The side-length of each tile r needs to fulfil the far-field condition

$$r < \sqrt{\frac{c \cdot d}{2f_{\mathrm{c},i}}}, \tag{21}$$

where d is the distance between the center of the tile and the terminal from which the wave is coming from. Then the electric field of a diffuse scattering path related to each tile at one subband i is calculated as

$$\begin{aligned} E_\mathrm{s}(f_{\mathrm{c},i}) =& A(f_{\mathrm{c},i})[\bar{g}_\mathrm{s}^{\mathrm{R}}(f_{\mathrm{c},i})]^* \cdot (\frac{dS\cos\vartheta_{\text{inc}}}{F_{\alpha_\mathrm{r}}})^{\frac{1}{2}} \cdot \\ & (\frac{1+\cos\varphi_\mathrm{r}}{2})^{\frac{\alpha_\mathrm{r}}{2}} \cdot [\bar{g}_\mathrm{s}^{\mathrm{E}}(f_{\mathrm{c},i})]\frac{SU}{s_\mathrm{s}s'_\mathrm{s}}e^{-j\theta_\mathrm{s}}E_0, \end{aligned} \tag{22}$$

where $s = s_\mathrm{s} + s'_\mathrm{s}$, s_s is the path length from Tx to the center of the tile, s'_s is the path length from the center of the tile to Rx, dS is the area of the tile, φ_r is the angle between the specular reflection direction and the scattering direction, α_r is an integer defined as the width of the scattering lobe, F_{α_r} is a function of α_r [12], S is the scattering coefficient, $U = |E_\mathrm{r}|/|E_\mathrm{i}|$ where $|E_\mathrm{r}|$ and $|E_\mathrm{i}|$ are the norms of the reflected and incident fields on the tile dS, and θ_s is a random phase component with an uniform distribution over $[0, 2\pi]$.

REFERENCES

[1] P. Meissner and K. Witrisal, "Analysis of position-related information in measured UWB indoor channels," in *Antennas and Propagation (EUCAP), 2012 6th European Conference on*, 2012, pp. 6–10.

[2] B. Alavi, N. Alsindi, and K. Pahlavan, "UWB channel measurements for accurate indoor localization," in *Military Communications Conference, 2006. MILCOM 2006. IEEE*, 2006, pp. 1–7.

[3] A. Molisch, "Ultrawideband propagation channels-theory, measurement, and modeling," *Vehicular Technology, IEEE Transactions on*, vol. 54, no. 5, pp. 1528–1545, 2005.

[4] H. Sugahara, Y. Watanabe, T. Ono, K. Okanoue, and S. Yarnazaki, "Development and experimental evaluations of "RS-2000" - a propagation simulator for UWB systems," in *Ultra Wideband Systems, 2004. Joint with Conference on Ultrawideband Systems and Technologies. Joint UWBST IWUWBS. 2004 International Workshop on*, May 2004, pp. 76 – 80.

[5] J. Jemai, P. Eggers, G. Pedersen, and T. Kürner, "On the applicability of deterministic modelling to indoor UWB channels," in *Proceedings of the 3rd Workshop on Positioning, Navigation and Communication (WPNC'06)*, 2006.

[6] V. Degli-Esposti, F. Fuschini, E. M. Vitucci, and G. Falciasecca, "Measurement and modelling of scattering from buildings," *Antennas and Propagation, IEEE Transactions on*, vol. 55, no. 1, pp. 143 – 153, Jan. 2007.

[7] G. Tiberi, S. Bertini, W. Malik, A. Monorchio, D. Edwards, and G. Manara, "Analysis of realistic ultrawideband indoor communication channels by using an efficient ray-tracing based method," *Antennas and Propagation, IEEE Transactions on*, vol. 57, no. 3, pp. 777 – 785, Mar. 2009.

[8] M. Gan, F. Mani, F. Kaltenberger, C. Oestges, and Z. T., "A ray tracing algorithm using the discrete prolate spheroidal subspace," in *IEEE International Conference on Communications (ICC)*, June 2013.

[9] C. Oestges, B. Clerckx, L. Raynaud, and D. Vanhoenacker-Janvier, "Deterministic channel modeling and performance simulation of microcellular wide-band communication systems," *Vehicular Technology, IEEE Transactions on*, vol. 51, no. 6, pp. 1422 – 1430, Nov. 2002.

[10] S. U. Inan and S. A. Inan, *Electromagnetic Waves*. Prentice, 2000.

[11] R. Luebbers, "Finite conductivity uniform GTD versus knife edge diffraction in prediction of propagation path loss," *Antennas and Propagation, IEEE Transactions on*, vol. 32, no. 1, pp. 70 – 76, Jan. 1984.

[12] F. Mani, F. Quitin, and C. Oestges, "Accuracy of depolarization and delay spread predictions using advanced ray-based modeling in indoor scenarios," *EURASIP Jounal in Wireless Commmunications and Networking*, vol. 2011, p. 11, 2011.

[13] P. Meissner, M. Gan, F. Mani, E. Leitinger, M. Froehle, C. Oestges, T. Zemen, and K. Witrisal, "On the use of ray tracing for performance prediction of UWB indoor localization systems," in *IEEE ICC 2013 Workshop on Advances in Network Localization and Navigation (ANLN)*, June 2013.

[14] R. Kouyoumjian and P. Pathak, "A uniform geometrical theory of diffraction for an edge in a perfectly conducting surface," *Proceedings of the IEEE*, vol. 62, no. 11, pp. 1448 – 1461, 1974.

[15] P. Meissner, E. Leitinger, M. Froehle, and K. Witrisal. (2013) MeasureMINT. [Online]. Available: http://www.spsc.tugraz.at/tools/UWBmeasurements

[16] S. Priebe, M. Jacob, and T. Kurner, "Calibrated broadband ray tracing for the simulation of wave propagation in mm and sub-mm wave indoor communication channels," *European Wireless, 2012. EW. 18th European Wireless Conference*, pp. 1 – 10, April 2012.